Naval welded joints local stress assessment and fatigue cracks monitoring with quantitative thermoelastic stress analysis

Loïc Carteron, Cédric Doudard, Sylvain Calloch, Bruno Levieil, J. Beaudet, F. Bridier

Naval welded joints local stress assessment and fatigue cracks monitoring with quantitative thermoelastic stress analysis

L. Carteron [a,b,*], C. Doudard [a], S. Calloch [a], B. Levieil [a], J. Beaudet [b], F. Bridier [b]

[a] *ENSTA Bretagne, UMR CNRS 6027, IRDL, 29200 Brest, France*
[b] *Naval Group, 5 rue de l'Halbrane, 44340, France*

Fatigue assessment of welded assemblies is a key challenge both for industrial and academic research. This paper assesses possibilities of thermoelastic coupling quantitative analysis for the comprehension of fatigue phenomena occurring with welded structures. A test protocol has been set up to measure temperature field on cruciform as- welded specimens under cyclic loading thanks to an infrared camera. Identification of temperature variations associated to thermoelastic coupling (order of magnitude of 0.1 K) allows to map temperature which are directly correlated to stress tensor first invariant. From this result, analysis of thermoelastic coupling gradient allows to determine the part of bending stress due to specimen distortion (up to 20% higher than nominal stress). Besides, thermal conduction influence when evaluating a local stress at weld toe is studied thanks to a numerical thermal model. In addition, infrared images post-treatment based on image segmentation is proposed for fatigue crack monitoring at weld toes (minimal crack size detection of 1 mm). Experimental validation is performed through analysis of marked fracture surface. Finally, fatigue crack growth rates are evaluated with this approach for different load amplitudes.

1. Introduction

Fatigue design of structures subjected to cyclic loading is a major concern for both industry and research since fatigue failure may represent up to 80% of in-service rupture cases [1]. In welded structures, larger risk of fatigue failure is located at the weld toe because of stress concentration, complex microstructure and possible weld defects. Understanding the heterogeneous stress field in this area is therefore a major concern when developing or using models for fatigue design.

Several full field experimental techniques exist to assess stress field at weld joints. Thermoelastic Stress Analysis (TSA) has become a recognized advantageous method to assess stress amplitude field on a surface under cyclic loading. Indeed, specimen tested under low stress cyclic loading (level significantly lower than the material elastic limit) shows cyclic temperature variations with the same frequency than loading and the temperature amplitude can be linked to the stress amplitude. The beginning and early development of TSA has been reviewed by Stanley [2]. This technique has been successfully applied to both standard specimens and more complex structures such as pressure vessels [3], fighter jet fuselage [4], power station drain lines [5] or additively manufactured aerospace brackets [6]. Other studies also have opened paths by experimenting this thermal approach on butt joints [7], thin steel sheet T-joint [8] and more complex welded structures such as a car wishbone [9]. Besides, temperature field study have also been used as a mean of fatigue crack monitoring [10] but only qualitative observations have been made. This paper aims to extract a maximum of quantitative informations from the temperature variation associated to thermoelastic coupling, on a specific configuration of joint, considered as a standard welded detail in naval industry.

This study faces several problematic and scientific challenges. On the one hand, the inherent stress heterogeneities implied around welded joints can be due to different aspects [11] such as weld toes geometry, residual stresses or welding defects. On the other hand, the use of a thermal approach may be complex and require precocious experimental measurements. Indeed, special cares need to be taken to obtain a reliable signal and some hypothesis need to be made to model the observed phenomena. Besides, thermal conduction in the metal will add difficulties since it may act as a leveller filter. This paper introduces the test protocol developed to perform infrared measurement on the studied welded specimen. Temperature evolutions during a fatigue test are then presented. Finally, results of TSA are discussed following two axes: (i) the evaluation of local stresses, and (ii) the detection and monitoring of fatigue cracks along weld toes. This last section proposes an infrared film

* Corresponding author at: ENSTA Bretagne, UMR CNRS 6027, IRDL, 29200 Brest, France.
E-mail address: loic.carteron@ensta-bretagne.org (L. Carteron).

Nomenclature

α	Isotropic expansion coefficient
$\Delta\theta_{the}$	Temperature amplitude associated with thermoelastic coupling
$\in$	Paint emissivity
Φ	Phase shift
ρ	Density
C	Heat capacity
f	Observed frequency
f_s	Loading frequency
I_{1amp}	Amplitude of the stress tensor first invariant
R	Load ratio
T_0	Initial temperature

post-treatment, an experimental validation and finally results comparison between two welded joint configurations. Conclusions and future insights end the paper.

2. Material and experimental set-up

This section introduces the specimens and the test protocol used during this study. Initial qualitative observations are then outlined through the analysis of thermal sequences during a fatigue test.

2.1. Studied specimens

Testing was carried out on cruciform non-load carrying welded joints (Fig. 1) made of DH36 naval grade steel (Yield stress of 360 MPa). Specimens were welded in Naval Group shipyard using Gas Metal Arc Welding (GMAW). Two types of specimen configurations were studied: as-welded joints and TIG-dressed specimen.

TIG dressing is based on remelting (with a TIG torch) the weld toes located between the main plate and the stiffeners. This process is used to increase fatigue life by enlarging weld toe radius and redistributing residual stresses around the weld area [12]. As-welded joints are the main focus of this article but TIG-dressed results will be introduced at some points in order to compare the two specimen configuration and identify differences in fatigue failure mechanism.

As a result of the welding procedure, all the studied samples have a slightly different degree of distortion (max +/−1 mm between middle profile of different free specimen). As previously observed in literature [11], samples present one face with a concave shape (Fig. 2) which therefore presents a higher stress level than the convex face when subjected to a tensile load. All the temperature observations have been carried out on the concave faces. The bending moment induced by this geometric distortion can be taken into account using a structural (or geometrical) stress approach. The use of structural stress as defined by the International Institute of Welding [11] allows to consider both the membrane and bending part of the stress applied to a welded joint. The structural stress is generally evaluated with finite element analysis or experimentally from interpolation of stress measurement performed with two strain gauges placed at 0.5 and 1.5 times the thickness from the weld toe [11]. In Section 3.2 thermoelastic coupling is used to assess the bending stress induced by specimen distortion.

2.2. Test set-up and equipment

Experiments have been performed on MTS® 250 kN tensile test machine with hydraulic clamping jaws (Fig. 3a). Repeated tensile loading with load ratio $R = F_{min}/F_{max} = 0.1$ has been applied for different stress amplitude levels, with a maximum nominal applied force smaller than the yield stress. Temperature field has been recorded using an infrared camera FLIR® SC7600MB with a 640×512 pixels sensor (Fig. 3b). Several thermal precautions have been taken to improve temperature measurement quality:

- Mat black painting (JELT® 5771) was applied on specimens in order to maximize the emissivity coefficient.
- A cooling system has been installed around clamping jaws to limit thermal drift during tests and to reduce the temperature gradient between the two clamps.
- A thick sheet has been placed around specimen and camera (Fig. 3a) to lower environmental influences that are convection and reflection.

Short videos of 200 s every 600 s have been recorded during fatigue tests until specimen failure. Pixel size is approximately 160 µm. FLIR® compensated calibration has been applied to each and every pixels to take in account the initial sensor temperature [13]. The smallest measurable temperature variation, also referred as Noise Equivalent Temperature Difference (NETD), of this camera is in the range of 20 mK. Camera frequency has been set to 1 Hz whereas mechanical loading frequency has been set to 10.02 Hz in order to observe thermoelastic cycles with the stroboscopic effect [14].

2.3. Temperature evolutions during fatigue test

As a first step, observation of the mean temperature (calculated over the framed part of the specimen) during a fatigue test (Fig. 3b) shows consistent results in terms of temperature evolution compared to observations reported in the literature on material specimen [15]. Two types of temperature variations can be noticed:

1. The cyclic variation of the signal may be identified and associated to the thermoelastic coupling effect [16].

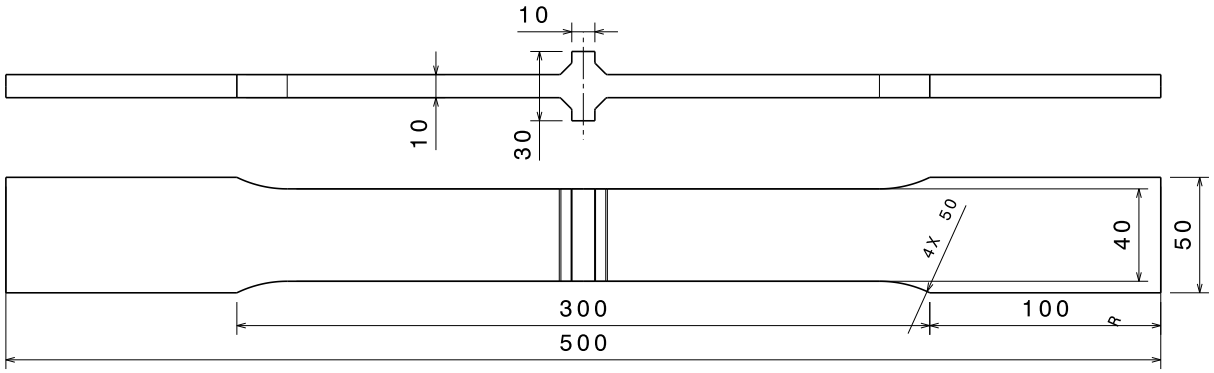

Fig. 1. Specimen geometry and dimensions.

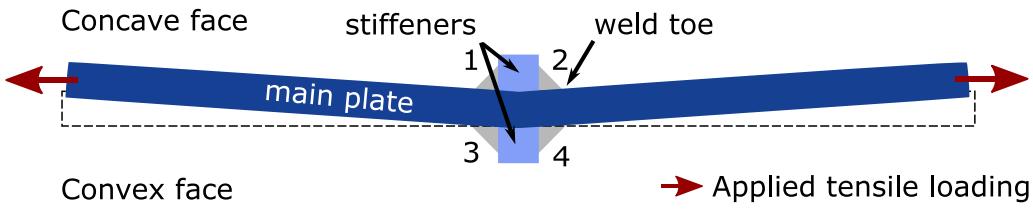

Fig. 2. Representation of specimen distortion induced by welding process.

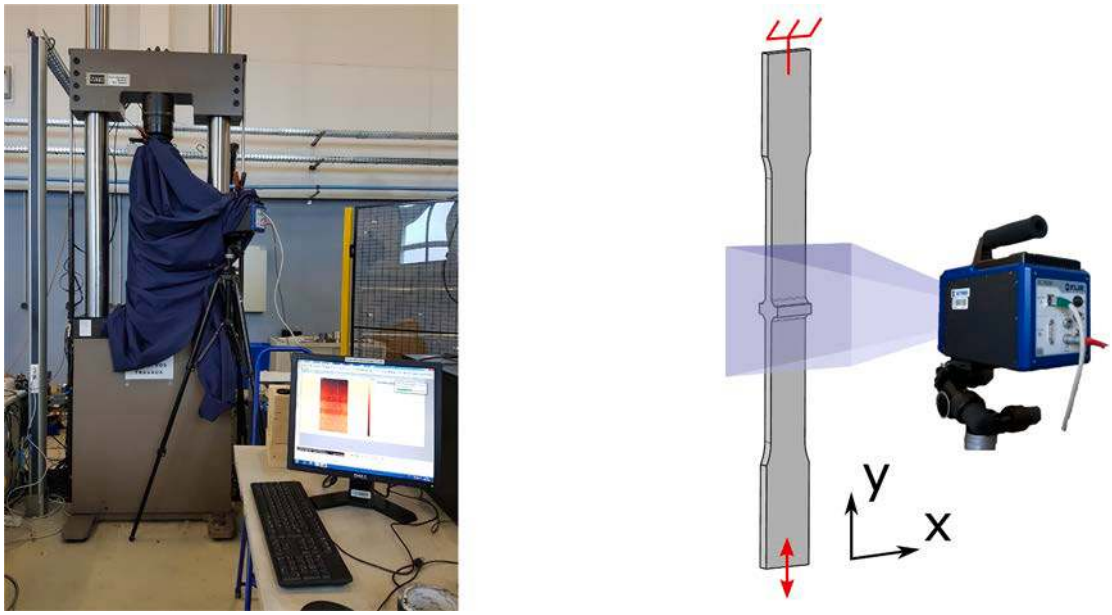

(a) Thermal isolation around clamping jaws and infrared camera

(b) Close-up of infrared camera framing

Fig. 3. Test set-up and equipment.

2. The mean thermal evolution which may be divided into three phases [17]: (i) a transient phase from 0 to $2{\cdot}10^4$ cycles where the global temperature increases, (ii) a steady-state phase from $2{\cdot}10^4$ cycles to $1.3{\cdot}10^5$ cycles where global temperature stays constant and (iii) a rapid increase prior to specimen failure from $1.3{\cdot}10^5$ cycles to the end of the test. Studies in the literature consider that the dissipation mechanism responsible for this temperature variation is micro-plasticity in the case of standard metal specimens [18]. In the case of welded structures, localized dissipation mechanisms may also be involved close to weld toes such as local plasticity or crack opening.

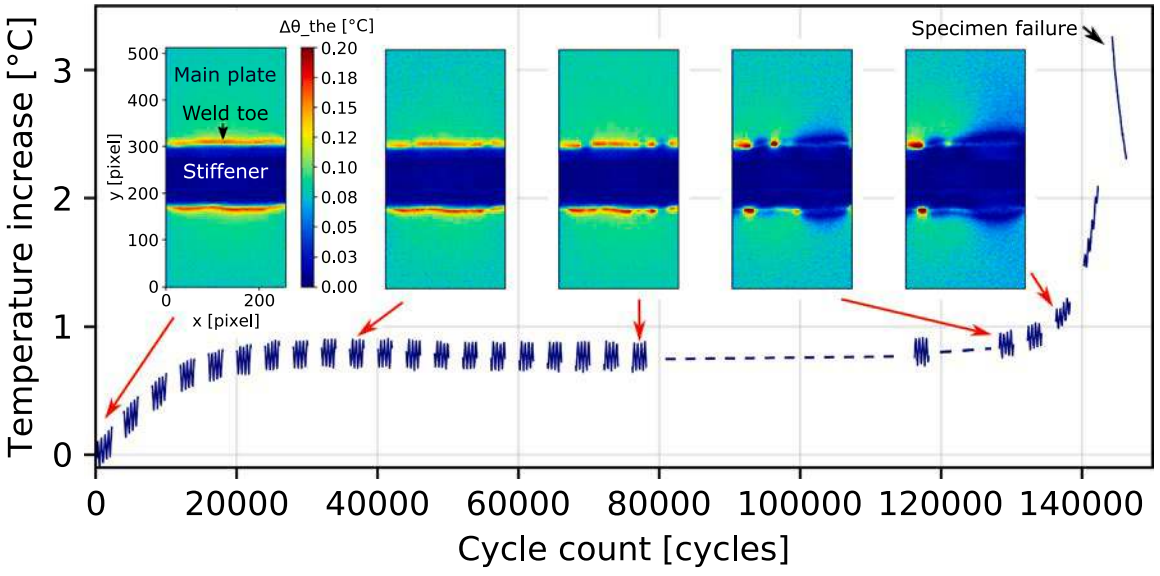

Fig. 4. $\Delta\theta_{the}$ map evolution monitored on as-welded specimen during fatigue test. Applied nominal stress amplitude is 115 MPa.

This article focuses exclusively on the informations that can be extracted from the analysis of thermoelastic coupling. Identification of the temperature amplitude associated with thermoelastic coupling, $\Delta\theta_{the}$, and a phase shift, ϕ, has been carried out on infrared data by fitting (least square optimization method) a function built as the sum of a shifted sine and a linear drift [19], such as:

$$F(t) = \Delta\theta_{the} sin(2\pi ft + \phi) + (At + B), \quad (1)$$

with A and B constants to be determined, and f the stroboscopic frequency (0.02 Hz). This identification has been performed for each pixel of each image of each infrared films, allowing the composition of $\Delta\theta_{the}$ maps (Fig. 4). Examination of the first $\Delta\theta_{the}$ map on Fig. 4 highlights the non-homogeneous stress field in this type of structure and shows that the stiffener displays a temperature amplitude $\Delta\theta_{the}$ close to zero as it is not directly submitted to the tensile load. Areas in red on $\Delta\theta_{the}$ map (Fig. 4) highlight concentrated stress areas located at the weld toes. Application of quantitative TSA [16] for the studied welded detail is introduced Section 3. The evolution of $\Delta\theta_{the}$ map during a fatigue test, mirrored with the averaged temperature evolution, is represented Fig. 4. Several interruptions of the red areas appear progressively during the test. These are indicators of fatigue cracks [7,10]. Quantitative analysis of this phenomena is proposed in Section 4. Fig. 4 highlights also that, for as-welded configuration, first cracks can be detected since the first third of the total life. By contrast, TIG dressed specimens show relatively short propagation phase (Fig. 5). This result supports the pertinence to consider the propagation phase in the total life estimation for as-welded joints whereas another approach is needed to model fatigue life of TIG dressed specimens. In the next sections, quantitative analysis of the experimental results will be proposed and discussed under two main axes: (i) quantification of local stresses at weld toes, and (ii) detection and monitoring of fatigue cracks along weld toes.

3. Local stresses quantification

This section introduces the benefits of the TSA method applied to the studied welded specimen. After underlining the equations of the thermoelastic phenomenon, the TSA is applied first to assess the bending stress induced by the specimen distortion and then to evaluate the local stress at the weld toes.

3.1. Thermoelastic stress analysis theory

The analysis of thermoelastic coupling is used as a technique to assess stress field on a surface. Indeed, under adiabatic hypothesis, the equation of thermoelasticity,links the amplitude of temperature variation associated to thermoelastic coupling heat source with the amplitude of stress tensor first invariant [20]. For an isotropic homogeneous material under a uniaxial loading, the heat source can be linked to the thermoelastic coupling such as,

$$S_{the} = -2\pi f_s \alpha T_0 I_{1amp} \cos(2\pi f_s t), \quad (2)$$

with f_s the loading frequency, α the isotropic expansion coefficient, T_0 the initial temperature and I_{1amp} the stress tensor first invariant amplitude. Assuming adiabaticity, the following expression can be written [9,21],

$$I_{1amp} = -\Delta\theta_{the} \frac{\rho C}{\epsilon \alpha T_0}, \quad (3)$$

where $\Delta\theta_{the}$ is the measured amplitude of the cyclic temperature evolution and ϵ the paint emissivity. Validity of the adiabatic hypothesis is discussed together with the influence of heat conduction in the forthcoming paragraph 3.3.

3.2. Assessment of bending stress induced by specimen distortion

The studied cruciform specimens have overall symmetrical geometry but initial distortion due to the welding process induces an additional bending stress during tensile tests. The use of TSA to quantify this additional part of the stress is evaluated in this paragraph. To validate the experimental results, a first finite element model has been implemented with the commercial software Abaqus to simulate only the mechanical behaviour of the specimens. Assuming two symmetry planes, only one fourth of the specimen geometry is considered and a driving force is applied at one end (Fig. 6). Initial distortion is introduced by setting the weld detail center offset of clamp axes by 0.75 mm (Fig. 6). This value has been measured onto the mean specimen profile thanks to in situ digital image correlation measurements when both ends of the specimen were clamped. Averaged connecting radius at the weld toes (Fig. 6) has been determined from a 3D scan of the chosen specimen (Values are given in Fig. 9). Connecting circle radius has been measured within +/−0.1 mm confidence. Material behavior is supposed elastic

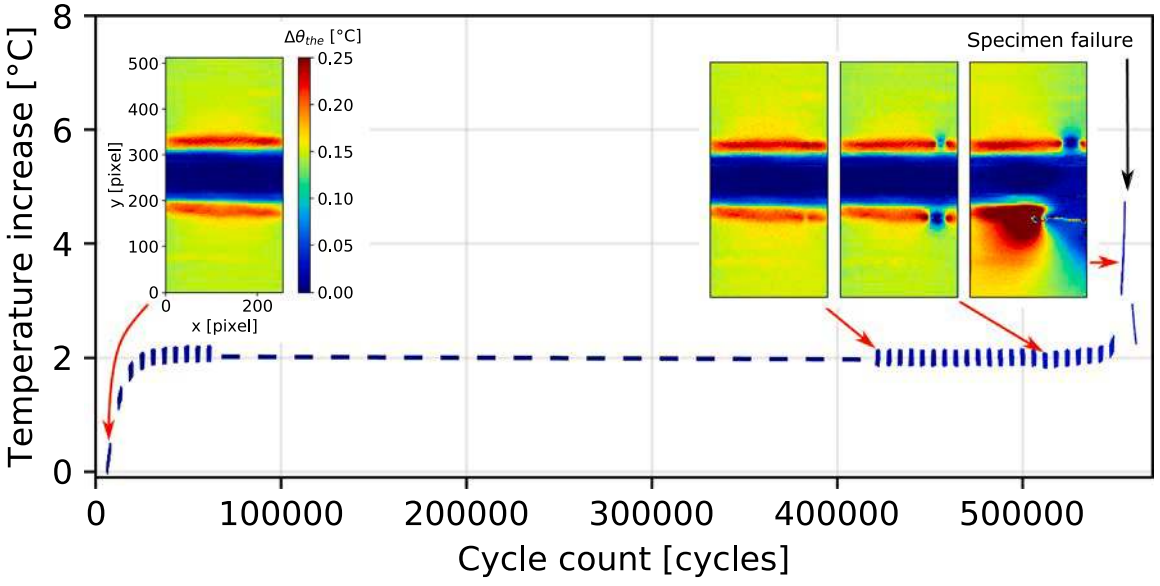

Fig. 5. $\Delta\theta_{the}$ map evolution monitored on TIG dressed specimen during fatigue test. Applied nominal stress amplitude is 150 MPa.

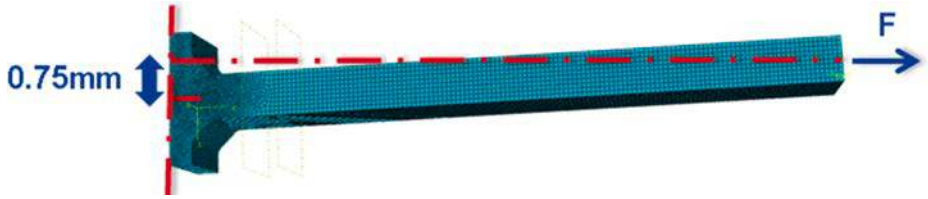

Fig. 6. Finite elements model mesh and boundary conditions.

and the specimen is meshed using C3D20R elements (20 nodes hexahedron with quadratic interpolation and reduced integration). The model uses 167080 elements including 60 elements located into the connecting radius of the studied weld toe. First stress invariant amplitude profile is extracted along the specimen central path and plotted in Fig. 7. For comparison purpose, experimental $\Delta\theta_{the}$ maps are projected along y axis (Fig. 7) assuming a signal average over ten pixels in the specimen middle ($\approx$ 1.6 mm). This value is a compromise between noise reduction by spatial average and side effects limitations. The coefficient $\frac{\rho C}{\epsilon \alpha T_0}$ introduced in Eq. (3) is calculated (1104 MPa $^{\circ}C^{-1}$) using the values in Table 1, a measured emissivity coefficient ϵ of 0.87, and a measured temperature T_0 of 293.15 K.

This coefficient is then applied to experimental temperature data (dots in Fig. 7)) to allow comparison with stress curve from the finite element model. Additional experimental points for validation have been obtained with four strain gauges (orange cross in Fig. 7). They have been positioned on the concave face, at approximatively once and twice the plate thickness from the weld toe. The strain gauge measure is then translated to stress measure under elastic hypothesis. Comparison between experimental data and mechanical finite element model result is shown Fig. 7. Fig. 7 highlights the good correlation between slopes of the experimental profile and the numerical model inside the intervals $abs(y) \in [20, 30]$ mm. This result confirms that thermoelastic coupling observations allow to capture and identify the influence of bending stress part caused here by the specimen distortion.

Furthermore, this infrared film analysis allows to define a custom structural stress from the $\Delta\theta_{the}$ profile. Fig. 8a illustrate the method. Then, by applying this approach to the same specimen for different load levels, Fig. 8b shows a linear evolution of structural stress versus nominal stress. For high stress levels, the difference between nominal and structural stress increases and becomes important. In conclusion, this approach allows to evaluate structural stress on welded specimen for a better description of the stress state close to the weld toe area.

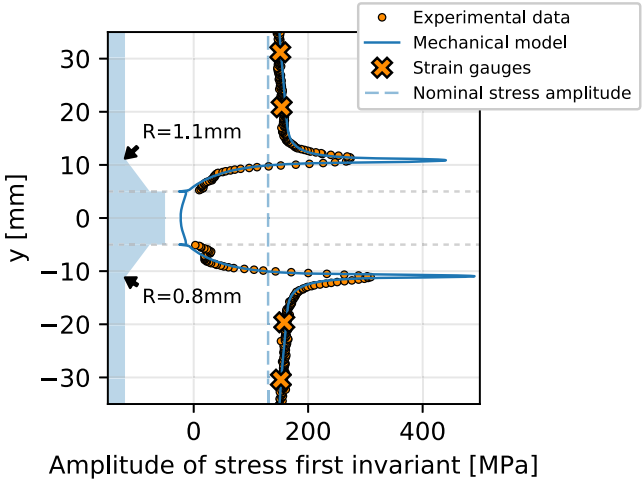

Fig. 7. Correlation between experimental results and mechanical finite element model.

Table 1
Measured thermomechanical constants for DH36 steel.

ρ [kg m^{-3}]	C [J kg^{-1} K^{-1}]	α [K^{-1}]
7803	426	$1.267.10^{-5}$

3.3. Local stress evaluation at weld toes

This paragraph focuses on how to evaluate the local stress at weld toe thanks to thermoelastic coupling analysis. Calculation of Fourier coefficient [20], defined as the ratio between conduction term and heating capacity, gives a value close to one in the local area of the weld toe. The heating capacity and the conduction part are thus of the same magnitude, meaning that the conduction of heat should be considered to increase the model quality. The stress field of the previous mechanical finite element model is thus reused in a second thermo-mechanical finite element model, with only the thermoelastic coupling as heat source. Stabilized temperature amplitude profile along specimen central path is extracted and represented on Fig. 9. A good correlation in the region of weld toes is obtained between experimental data and thermo-mechanical model curve. With this technique, the weld toe local stress analysis allows to catch the influence of the connecting radius over the stress concentration. Indeed, the smaller the radius, the higher the concentration stress. Therefore, this approach may also be used to evaluate an equivalent weld toe radius despite the difficulty to determine a unique radius. Besides, a perspective to increase the $\Delta\theta_{the}$ peaks intensity might be to increase the loading frequency. However, the paint thickness influence would the have to be considered [9].

4. Fatigue crack detection and monitoring

Observation of the thermoelastic coupling may also serve for damage evolution monitoring in composite materials [22] or fatigue crack monitoring [10]. Ummenhofer et al. have also explored the possibility to use this approach to monitor cracks on butt weld joints [7]. They have shown that $\Delta\theta_{the}$ evolve towards zero where cracks appear which is logical as there is no material to support a stress. Quantification of the cracks size is proposed in this section thanks to a post-treatment based on image processing. A validation of the method is then outlined before further observations of crack growth rates.

4.1. Infrared films post-treatment

Firstly, selection of a smaller working area (4 $\times$ 40 mm) around studied weld toes is performed to reduce processing time. The next step is the application of a 3 by 3 pixels median filter in order to reduce white noise and to smooth the images (Fig. 10). Images from Fig. 10 represent the evolution of $\Delta\theta_{the}$ map on one specimen weld toe during fatigue test. First image 10(a) shows the initial state where the blue to green areas are associated to the base plate of the specimen and the red pixels are associated to the stress concentration at the weld toe. No cracks are significantly visible at this stage. Then, on the next image 10(b), several cracks can be easily detected by visual inspection. The last picture 10(c) finally shows the propagation of several cracks and coalescence of two close cracks. The goal of the proposed post-treatment is to automatize

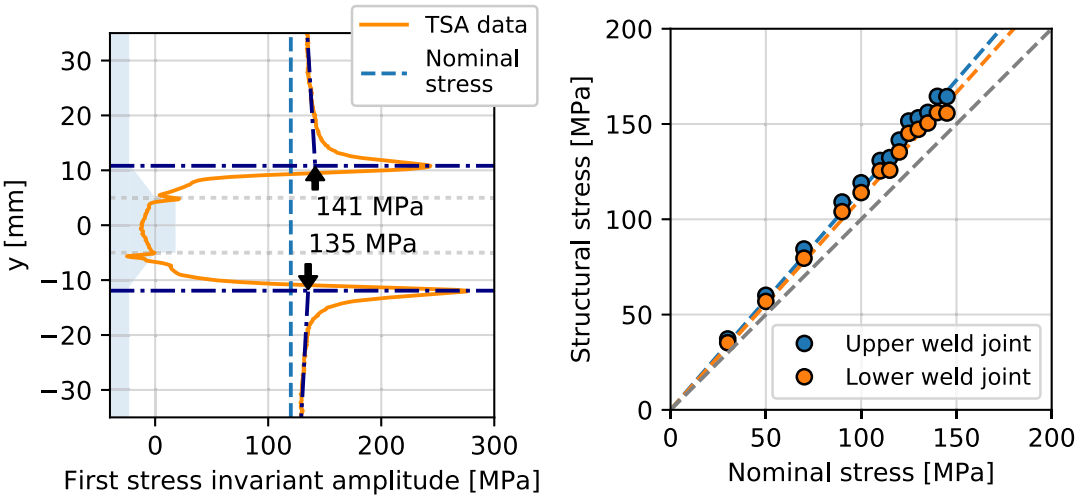

(a) Structural stress evaluation by interpolation of $\Delta\theta_{the}$ profile at weld toe peak

(b) Structural stress evolution versus nominal stress applied (on same specimen)

Fig. 8. Structural stress assessment from infrared data analysis.

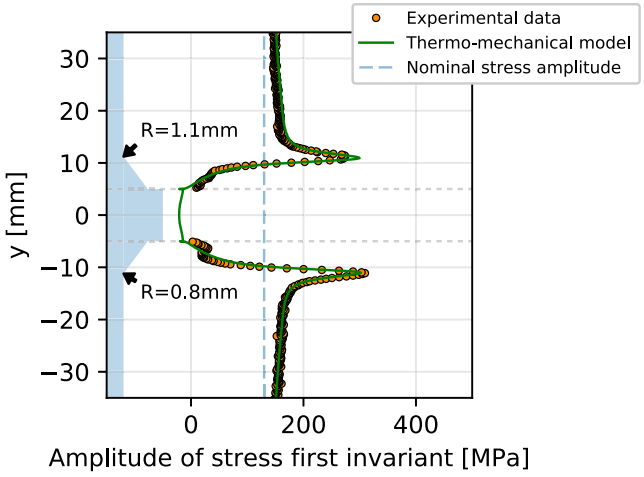

Fig. 9. Correlation between experimental results and thermo-mechanical model.

this analysis and to allow quantitative monitoring of crack propagation along weld toes.

Histogram of images from Fig. 10 are overlayed in Fig. 11. These histograms show relatively low contrast. Observation of initial histogram, in blue, shows one main peak corresponding to main plate pixels. Pixels associated to the weld toe stress concentration area, located at the right hand side of the histogram, are not numerous. Comparison of the three histograms shows that image contrast is increasing during fatigue test. Indeed, crack propagation involve both darker pixels occurrence in cracked areas and stress increase in healthy areas.

Several segmentation algorithm have been experimented on $\Delta\theta_{the}$ maps. Edges detection segmentation approaches don't supply satisfactory results because of low contrast images where no important gradient allows easy edges detection. Segmentation methods based on morphological operations also have been excluded because they may damage the data and affect crack size characterisation.

The chosen segmentation method is based on thresholding. Segmentation results of previous images from Fig. 10 are displayed in Fig. 12. Ostu's algorithm for automatic detection of optimal threshold [23] also have been experimented but doesn't give good results in this

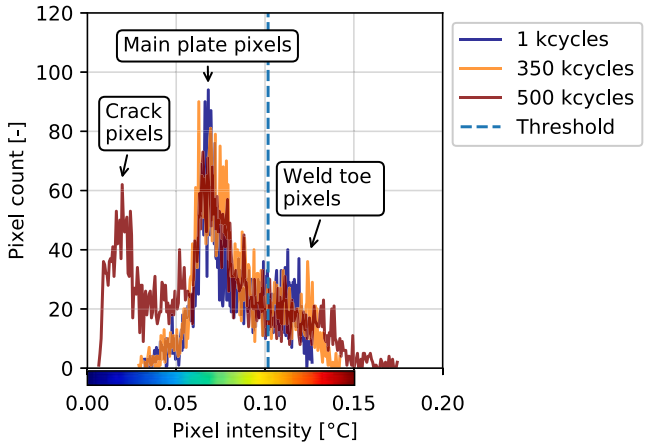

Fig. 11. Overlay of images histogram from Fig. 10.

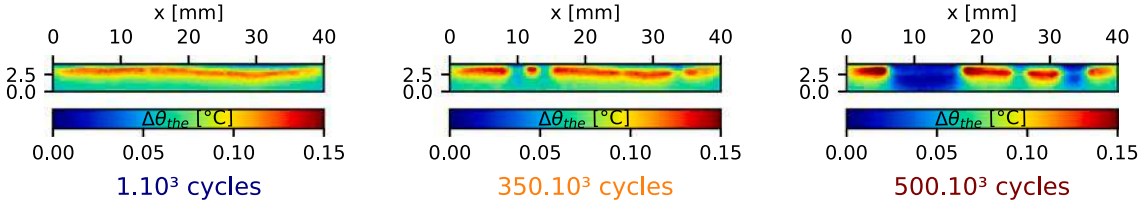

(a) (b) (c)

Fig. 10. Evolution of $\Delta\theta_{the}$ map (cropped over lower weld toe) during fatigue testing of Specimen No.3.

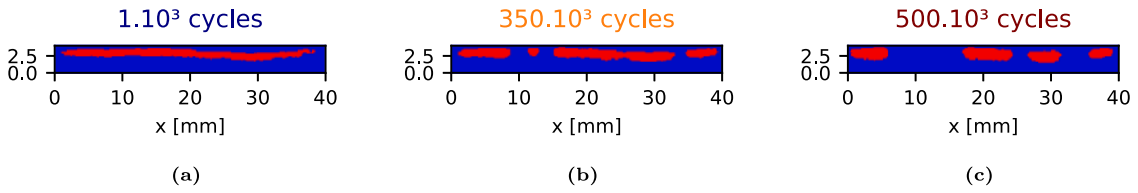

Fig. 12. Image segmentation of images from Fig. 10 using thresholding.

configuration because of no clear presence of second peak in the high intensity pixels. The threshold is here determined from the first $\Delta\theta_{the}$ map of fatigue test and kept constant for all images. Its value is determined by calculating the average maximum pixel intensity and the position of main peak. Sensitivity of this threshold value is discussed in the next section.

The last step of the post-treatment consists in labelling the segmented images. Different values are given to each separated image areas. Quantification of the cracks size is then extracted thanks to the bounding box properties of the labelled areas. The output of one short infrared film is therefore a one dimension equivalent welded joint associated to a certain number of cycles. Fig. 13 shows the post-treatment output of the three initial images introduced in Fig. 10.

By vertically stacking these one dimension equivalent joints, a picture of the crack growth history during fatigue tests can be plotted. To illustrate this operation, the three images from Fig. 13 are highlighted with dashed lines in Fig. 14c. Fig. 14 introduces result of proposed post-treatment obtained for five different specimens loaded at different levels and a result obtained on a TIG dressed specimen for comparison. Analysis of these images allows some well-known observations and points out worth-noting facts:

- Cracks as small as 1 mm can accurately be detected and coalescence of cracks can be monitored.
- Propagation represents at least half of the specimen fatigue life.
- When the stress is increased, the number of cracks increases too.
- This post-treatment may not detect small cracks located around the edges of the specimen due to side effect (Fig. 14e).
- Some crack starts to propagate later than other, which might be explained by different weld toe geometrical criticality or different initial defects sizes (not detected by bleeding).
- Fewer cracks are detected on TIG dressed specimens. Coalescence has therefore no time to impact fatigue life. Propagation phase represent a small fatigue life part of this specimen configuration.

4.2. *Output sensitivity to threshold value*

Sensitivity to threshold value has been studied to ensure approach reliability. Fig. 15 shows three segmentation results of the same initial image introduced in Fig. 4(c) with 10% variation of threshold value. These results emphasize a low sensibility to the threshold value.

Threshold sensitivity can also be observed onto complete fatigue test output. Fig. 16 allows comparison of output for three different threshold values. The three images show globally similar shapes. Three comparison criteria may be considered:

- First cracks detection: Threshold value has a non negligible influence on small crack detection capacity (see Table 2). In addition, when threshold is too high, artefacts appear with no physical significance (Fig. 16c) Therefore, cracks below 1 mm cannot be reliably detected with the proposed approach. Nevertheless, this information will not be used in the next section analysis.
- Final cracks size: Final crack size differences are lower than 5% for cracks larger than 4 mm and less than 2% for cracks larger than 10 mm. Threshold value has therefore a very limited influence here.
- Crack growth rate: Yellow shapes geometry appear comparable and crack growth rates estimated in Table 3 show low sensibility to threshold.

4.3. *Post-treatment validation: fracture surface analysis*

Experimental validation has been carried out by performing interrupted fatigue test on four specimens. After interruption, standard bleeding has not shown any evidence of cracks. Thus, specimens have been placed into a furnace at 500 °C during 30 min in order to mark all free surfaces including fatigue cracks. Specimen opening has then been carried out through cycling loading with through thickness pre-cut when needed (as can be seen, for example, on fracture surface in Fig. 17b). Cracks appear marked with black on fracture surfaces in Fig. 17. The crack position detected with infrared image processing correlate well with the marked surfaces. Moreover, a good correspondence is also found when observing coalescence locations. Crack width measurements have been performed thanks to numerical microscope.

These measures have been compared to the output of $\Delta\theta_{the}$ maps processing in Fig. 18. Maximum differences are within 15% along the whole range of detected crack sizes.

Fracture surface analysis provided several justifications:

- Fatigue cracks evolve faster towards edges than through the thickness which can be explained by inhomogeneous stress field in specimen thickness,
- Proposed infrared image processing allows good estimation of cracks position and width.

4.4. *Crack growth rate observations*

Representation of crack size evolutions before coalescence has been plotted in Fig. 19. Only one main crack size evolution per specimen and per stress level has been plotted to keep graph light and clear. Influence of stress level is in good agreement with expectations: the higher the stress level, the faster the crack propagates. In addition, the crack size

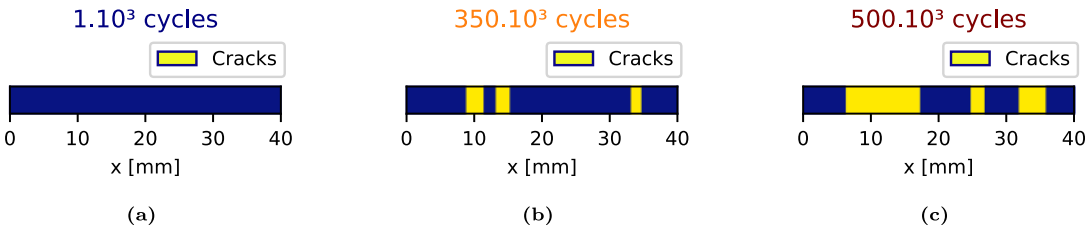

Fig. 13. Post-treatment output: one-dimension equivalent weld toe with cracked areas.

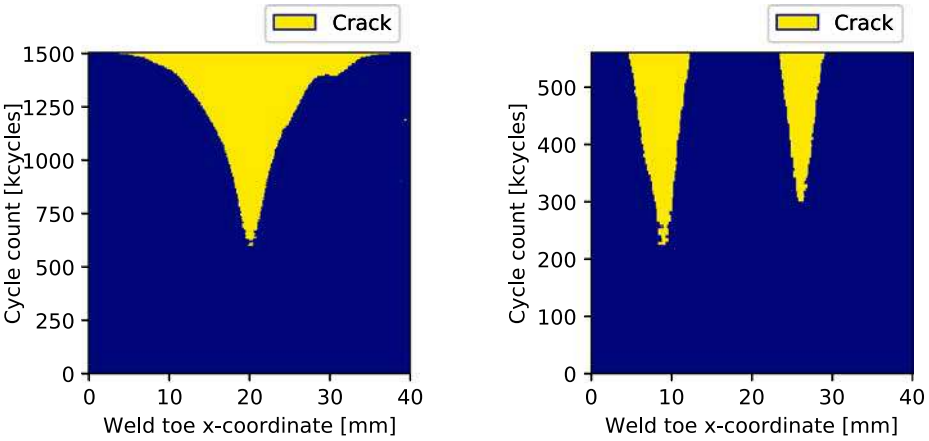

(a) As-welded specimen No.1
σ_{amp}^{nom}: **70 MPa**
Failure at 1,507,455 cycles

(b) As-welded specimen No.2
σ_{amp}^{nom}: **80 MPa**
Failure at 565,473 cycles

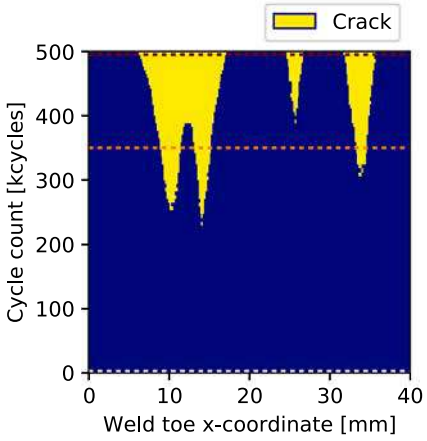

(c) As-welded specimen No.3
σ_{amp}^{nom}: **90 MPa**
Interruption at 500,000 cycles

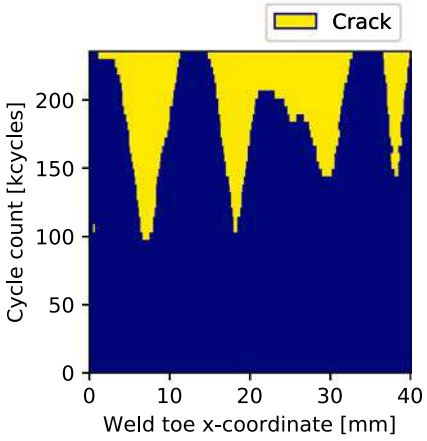

(d) As-welded specimen No.4
σ_{amp}^{nom}: **110 MPa**
Failure at 236,604 cycles

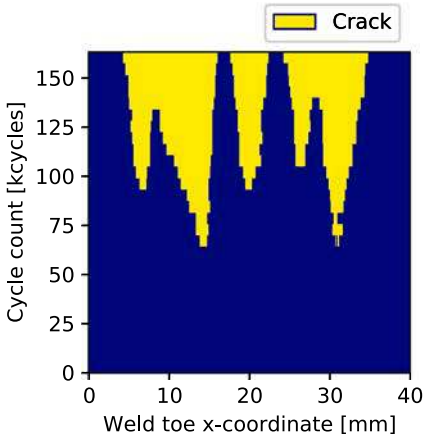

(e) As-welded specimen No.5
σ_{amp}^{nom}: **110 MPa**
Failure at 161,629 cycles

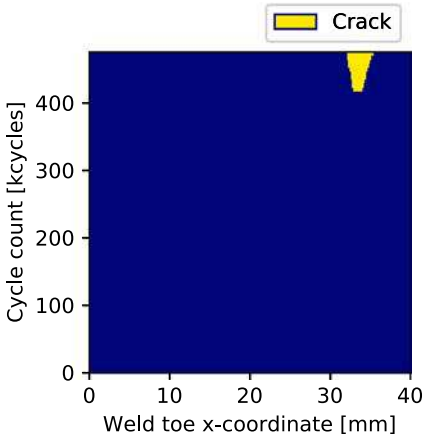

(f) **TIG dressed** specimen
σ_{amp}^{nom}: 150 MPa
Failure at 549,167 cycles

Fig. 14. Post-treatment output of five as-welded specimen loaded at different stress level and one TIG-dressed specimen. Horizontal dotted lines on Figure (c) correspond to 1D welds of Fig. 13.

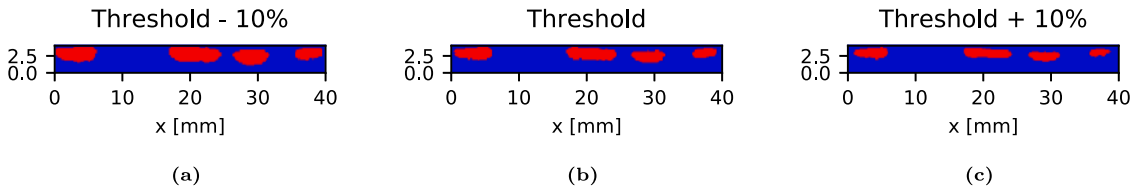

Fig. 15. Segmentation sensitivity to threshold (Specimen No.3 at 500 kcycles).

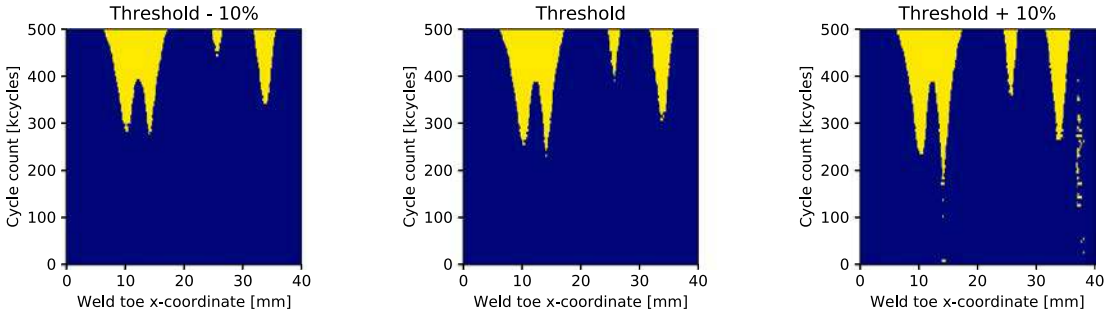

Fig. 16. Final output sensitivity to threshold (Specimen No.3).

Table 2
Crack size monitoring sensitivity to threshold considering only specimen No.3 leftmost crack propagation.

	Cycle count [kcycles]	300	350	400	450	500
Crack size [mm]	Threshold −10%	1.2	2.2	6.9	8.4	10.7
	Threshold	1.7	2.6	7.3	8.8	10.9
	Threshold +10%	2.0	2.8	7.5	9.0	11.1

Table 3
Crack growth rate estimated by finite differences from Table 2.

	Cycle count [kcycles]	325	375	425	475 0
Crack growth rate [mm/cycles]	Threshold −10%	2.e-5	9.4e-5	3e-5	4.6e-5
	Threshold	1.8e-5	9.4e-5	3e-5	4.2e-5
	Threshold +10%	1.6e-5	9.4e-5	3e-5	4.2e-5

evolution is mostly linear after 1 mm. Crack size growth rate may therefore be considered constant over time. Linear regression has been carried out to estimate crack growth rate as a single value for each nominal stress level (Fig. 20).

Representation of crack growth rate versus geometric stress is shown in logarithmic scale in Fig. 20. It underlines that points may be modelled with a slope of 4.1. Geometric stress amplitude is consider here to reduce variability induced by specimen distortion and is determined thanks to earlier introduced TSA approach (Section 3.2).

4.5. Initiation criterion for fatigue test campaign analysis

Conventional fatigue tests have been performed with additional use of infrared camera. The proposed post-treatment has then be used to determine an initiation criterion. Both failure criterion and 2 mm initiation criterion are used in Fig. 21 to analyse fatigue tests data. This figure highlights the fact that main fatigue life of the cruciform as-welded joints correspond to propagation phase. Besides, Basquin model has been identified to model traditional fatigue points. A slope of 3.9 is calculated for the mean curve. This value appears to be of the same magnitude order that the slope found in Fig. 20 (slope of 4.1). This observation adds another argument to the fact that crack propagation correspond to the main part of fatigue mechanism for the studied type of as-welded joints. In comparison, fatigue results of TIG dressed specimens show a different Basquin slope of 6 and considering the 2 mm initiation criteria doesn't affect the mean curve such as with as-welded configuration.

5. Conclusions

Experimental set-up has been developed to study naval grade steel welded joint under cyclic loading with an infrared camera. Cyclic temperature variations associated to thermoelastic coupling have been studied following two main axis:

1. The first one is the application of TSA approach. It offers a powerful tool for welded joint study as:
   (a) Stress gradient associated to bending stress induced by specimen distortion can be quantified (Geometric stress may be up to 20% higher than nominal stress).
   (b) A local stress at weld toe may be evaluated (Stress concentration factor between 2 and 3).
   (c) Influence of weld toe radius is visible even if heat conduction acts as a leveller filter.
2. Second axis is the development of an infrared image post-treatment, based on segmentation, for fatigue crack monitoring.
   (a) This approach was first experimentally validated thanks to marked fracture surface observations. The following conclusions have been made:
      i. Proposed infrared images post-treatment shows good agreement with crack sizes measured on marked fracture surfaces.
      ii. Threshold influences crack size detection within +/−0.3 mm precision range, whereas threshold does not significantly impact crack growth rate monitoring
   (b) Application of the proposed post-treatment to study as-welded and TIG dressed specimens allows several observations to be made:

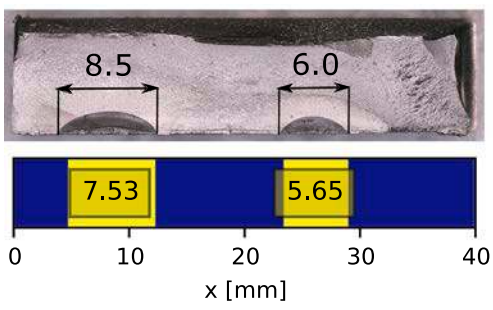

(a) Specimen No.2, σ_{amp}^{nom}: **80 MPa**
Failure at 565,473 cycles

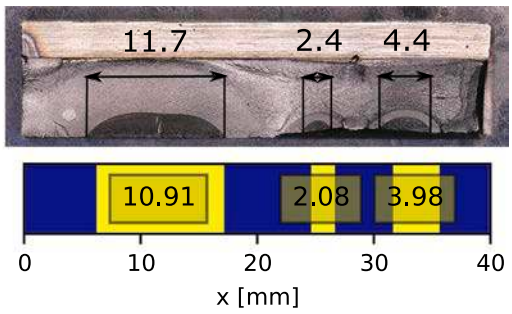

(b) Specimen No.3, σ_{amp}^{nom}: **90 MPa**
Failure at 500,000 cycles

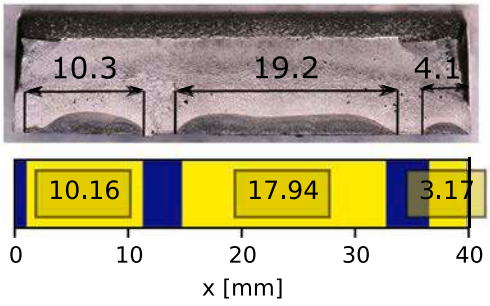

(c) Specimen No.4, σ_{amp}^{nom}: **110 MPa**
Failure at 236,604 cycles

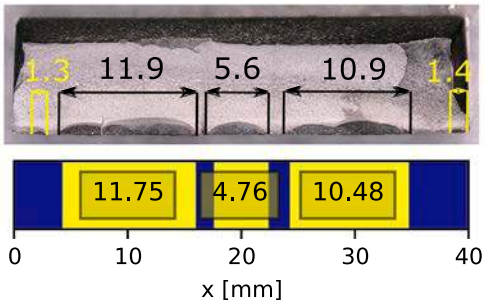

(d) Specimen No.5, σ_{amp}^{nom}: **110 MPa**
Failure at 161,629 cycles

Fig. 17. Post-treatment output of five specimen loaded at different stress level with juxtaposition of marked fracture surface.

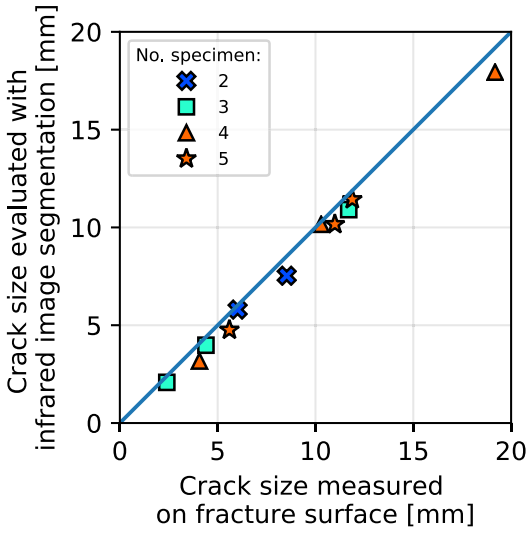

Fig. 18. Experimental validation of post-treatment.

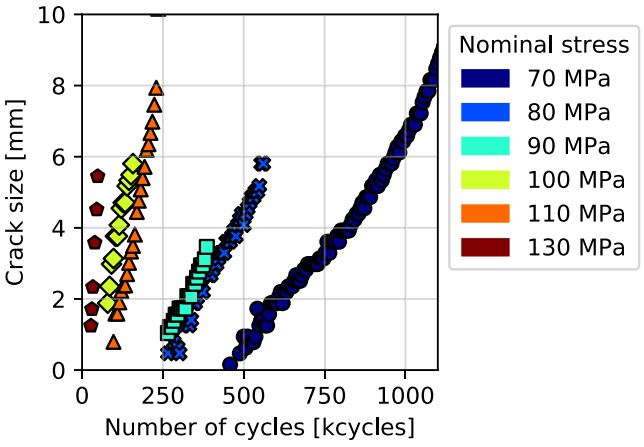

Fig. 19. Crack width evolution evaluated from $\Delta\theta_{the}$ maps processing.

i. When the stress is increased, the number of cracks increases too (from 1 crack initiated at 70 MPa to 5 cracks initiated at 110 MPa)
ii. When the stress is increased, the crack growth rate increases too. A slope of 4.1 is found between crack growth rate and the geometric stress
iii. The crack growth rate does not significantly evolve with crack size
iv. With as-welded joints, multi-site crack initiation are captured along weld toe, whereas TIG dressed specimens show in average only one crack propagation per weld seem.
v. Crack coalescences can be observed on as-welded joints.
vi. For as-welded configuration, propagation phase corresponds to more than half of the fatigue life, whereas propagation phase represents only a short fatigue life part of TIG dressed specimens.

This database of observations, collected exclusively through thermoelastic coupling study, may potentially be used as an identification base for future modelling works. In addition, all the informations that can be extracted from the thermoelastic coupling is only one part of the data contained in the infrared films. Temperature raise associated to dissipation may also be studied allowing more informations to be collected.

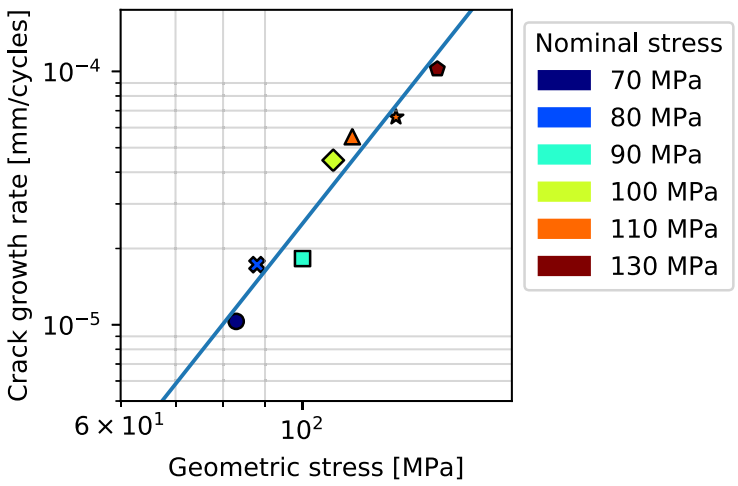

Fig. 20. Crack growth rate estimated from linear regression of Fig. 20 curves versus geometric stress determined by $\Delta\theta_{the}$ 1D profil processing.

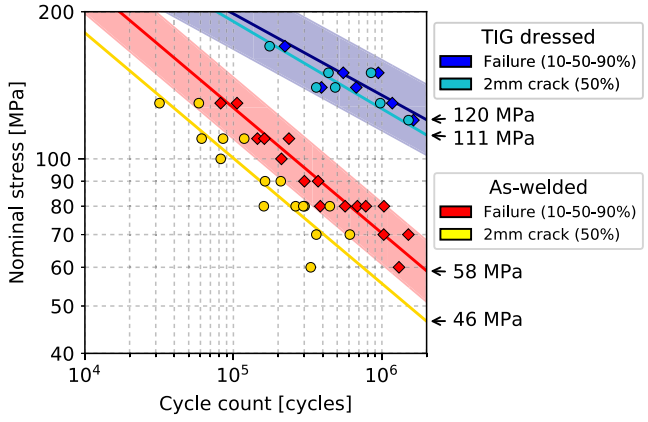

Fig. 21. Conventional fatigue tests results analysed with proposed post-treatment.

Declaration of Competing Interest

The authors declare that they have no known competing financial interests or personal relationships that could have appeared to influence the work reported in this paper.

References

[1] M.D. Sangid, The physics of fatigue crack initiation, Int. J. Fatigue 57 (2013) 58–72, https://doi.org/10.1016/j.ijfatigue.2012.10.009.

[2] P. Stanley, Beginnings and early development of thermoelastic stress analysis, Strain 44 (4) (2008) 285–297, https://doi.org/10.1111/j.1475-1305.2008.00512.x.

[3] P. Stanley, Applications and potential of thermoelastic stress analysis, J. Mater. Process. Technol. 64 (1–3) (1997) 359–370, https://doi.org/10.1016/S0924-0136(96)02587-3. URL https://www.sciencedirect.com/science/article/pii/S0924013696025873.

[4] N. Rajic, S.C. Galea, D. Rowlands, Thermoelastic stress analysis - emerging opportunities in structural health monitoring, Key Eng. Mater. 558 (2013) 501–509, https://doi.org/10.4028/www.scientific.net/KEM.558.501. URL https://www.scientific.net/KEM.558.501.

[5] R. Tighe, G. Howell, J. Tyler, S. Lormor, J. Dulieu-Barton, Stress based non-destructive evaluation using thermographic approaches: From laboratory trials to on-site assessment, NDT E Int. 84 (2016) 76–88, https://doi.org/10.1016/J.NDTEINT.2016.08.005. URL https://www.sciencedirect.com/science/article/pii/S0963869516300767.

[6] G. Allevi, M. Cibeca, R. Fioretti, R. Marsili, R. Montanini, G. Rossi, Qualification of additively manufactured aerospace brackets: A comparison between thermoelastic stress analysis and theoretical results, Meas. J. Int. Meas. Confed. 126 (May) (2018) 252–258, https://doi.org/10.1016/j.measurement.2018.05.068.

[7] T. Ummenhofer, J. Medgenberg, On the use of infrared thermography for the analysis of fatigue damage processes in welded joints, Int. J. Fatigue 31 (1) (2008) 130–137, https://doi.org/10.1016/j.ijfatigue.2008.04.005.

[8] D. Chen, S. Sun, J. Dulieu-Barton, Q. Li, W. Wang, Crack growth analysis in welded and non-welded T-joints based on lock-in digital image correlation and thermoelastic stress analysis, Int. J. Fatigue 110 (November 2017) (2018) 172–185. doi:10.1016/j.ijfatigue.2018.01.020.

[9] P. Florin, C. Doudard, M. Facchinetti, S. Calloch, Determination of the first stress tensor invariant of a complex steel sheet structure from Thermoelastic Stress, Analysis 133 (2015) 736–745, https://doi.org/10.1016/j.proeng.2015.12.655.

[10] J.a. Charles, F.J. Appl, J.E. Francis, Using the scanning infrared camera in experimental fatigue studies, Exp. Mech. 15 (4) (1975) 133–138, https://doi.org/10.1007/BF02318849.

[11] A. Hobbacher, Recommendations for Fatigue Design of Welded Joints and Components. IIW document IIW-2259-15, 2016.

[12] H.C. Yildirim, Review of fatigue data for welds improved by tungsten inert gas dressing, Int. J. Fatigue 79 (2015) 36–45, https://doi.org/10.1016/j.ijfatigue.2015.04.017. URL http://linkinghub.elsevier.com/retrieve/pii/S0142112315001334.

[13] V. Le Saux, C. Doudard, Proposition of a compensated pixelwise calibration for photonic infrared cameras and comparison to classic calibration procedures: Case of thermoelastic stress analysis, Infrared Phys. Technol. 80 (2017) 83–92, https://doi.org/10.1016/j.infrared.2016.11.008.

[14] P. Florin, M. Facchinetti, C. Doudard, S. Calloch, Fast fatigue properties identification by self-heating method: Application to automotive welded joints, Procedia Eng. 66 (2013) 676–683, https://doi.org/10.1016/j.proeng.2013.12.120.

[15] R. Blotny, J. Kaleta, A method for determining the heat energy of the fatigue process in metals under uniaxial stress: Part 1. Dtermination of the amount of heat liberated from a fatigue-tested specimen, Int. J. Fatigue (1986).

[16] P. Stanley, W. Chan, A new experimental stress analysis technique of wide application, in: Exp. Stress Anal., Springer, Netherlands, Dordrecht, 1986, pp. 479–487, https://doi.org/10.1007/978-94-009-4416-9_52. URL http://www.springerlink.com/index/10.1007/978-94-009-4416-9_52.

[17] G. La Rosa, A. Risitano, Thermographic methodology for rapid determination of the fatigue limit of materials and mechanical components, Int. J. Fatigue 22 (1) (2000) 65–73, https://doi.org/10.1016/S0142-1123(99)00088-2.

[18] C. Doudard, S. Calloch, F. Hild, P. Cugy, A. Galtier, Identification of the scatter in high cycle fatigue from temperature measurements (2004). https://hal.archives-ouvertes.fr/hal-00002927/document.

[19] J.-C. Krapez, Compared performances of four algorithms used for modulation thermography, Proc. 1998 Int. Conf. Quant. InfraRed Thermogr. 1 (1) (1998). doi: 10.21611/qirt.1998.023. http://qirt.org/archives/qirt1998/papers/023.pdf.

[20] M.A. Biot, Thermoelasticity and irreversible thermodynamics, J. Appl. Phys. 27 (3) (1956) 240–253, https://doi.org/10.1063/1.1722351.

[21] G. Pitarresi, A review of the general theory of thermoelastic stress (2003). doi: 10.1243/03093240360713469.

[22] T. Emery, J. Dulieu-Barton, Thermoelastic Stress Analysis of damage mechanisms in composite materials, Compos. Part A Appl. Sci. Manuf. 41 (12) (2010) 1729–1742, https://doi.org/10.1016/j.compositesa.2009.08.015. URL https://www.sciencedirect.com/science/article/pii/S1359835X09002413.

[23] N. Otsu, A Tlreshold Selection Method from Gray-Level Histograms C (1) (1979) 62–66.